Experimental and computational analysis of elastomer membranes used in oscillating water column WECs

Farhad Abad [*], Saeid Lotfian, Saishuai Dai, Guangwei Zhao, Guillermo Idarraga Alarcon, Liu Yang, Yang Huang, Qing Xiao, Feargal Brennan

Faculty of Engineering, University of Strathclyde, Glasgow, G4 0LZ, UK

A B S T R A C T

The study investigates the structural characterisation of flexible membranes used in oscillating water column (OWC) wave energy converters (WECs). Four commonly utilised elastomers – natural rubber, nitrile rubber, silicone, and latex – were subjected to a novel hyperelastic model selection process. A custom bulge test setup enabled the selection of second-order Mooney-Rivlin (SOMR) and Yeoh models for relevant accuracy (RMSE<0.018 MPa), stability and numerical validation. A 1:20 scale OWC model with latex was tested in a water tank to examine the effects of waves with a frequency range of 0.25–1.4 Hz and up to 0.24m amplitude. Water tank experiments demonstrated smooth frequency responses for OWC with membrane, beneficial for consistent power generation. A dry test rig was designed and built to replicate OWC inflation conditions and apply cyclic loadings up to 1.5 Hz, overcoming pressure limitations of the water tank, exploring wider material options, and validating numerical simulation. An optical motion capture system, Qualisys, supported the validation process by providing precise data on membrane deformation during experiments. Furthermore, finite element analysis (FEA) was utilised to conduct stress analysis and parametric studies, assessing the suitability of these materials for flexible OWC application.

1. Introduction

WECs have emerged as a promising technology for generating electricity from ocean waves, offering a reliable and sustainable energy source to support the global shift towards renewable energy [1]. The OWC is a WEC type that offers several advantages, such as simple geometry, high reliability and easy maintenance [2], over others, making it one of the most preferred options among available WECs [3,4]. This device includes an air chamber to convert wave motion into air pressure and a power take-off (PTO) system to convert pneumatic power into electricity [5]. Various PTO mechanisms, such as bidirectional and impulse turbines, have been proposed and explored for the OWC technology [6,7]. Recently, there has been an increased focus on dielectric elastomer generators (DEGs) as a solution to technical issues related to the limited adaptability of turbines in harsh sea environments [8,9]. Dielectric elastomers (DE) are rubber-like dielectrics used as actuators, generators, and sensors in various applications [10,11], particularly when large deformations are required. Exploring elastomers in OWCs has emerged as a promising field of study, primarily due to the

remarkable mechanical properties of elastomers, which allow for significant deformation under stress. Fig. 1 shows a schematic diagram of the novel flexible OWC and its integration with dielectric elastomer generators (DEGs).

Li and Xiao [12] developed a fully coupled fluid-structure interaction (FSI) model for an OWC with flexible materials. They showed that using hyperelastic material increases the efficiency of the OWC compared with using linear-elastic materials. An accurate and stable hyperelastic model, which can be distinguished by their unique strain energy functions [13], must be found to investigate the impact of elastomers on WECs. Specific hyperelastic models such as the Neo-Hookean, Mooney-Rivlin [14], and Ogden [15] may exhibit better stability and suitability depending on the material and loading conditions. For instance, the Ogden hyperelastic model is superior to other models in describing highly compressible foam deformation, particularly under significant stretching [16]. There are various methods to identify the appropriate hyperelastic models, including the gradient method [17], a mixed experimental and numerical approach [18], and inverse material characterization [19]. Standard tests like the tensile, compression, biaxial,
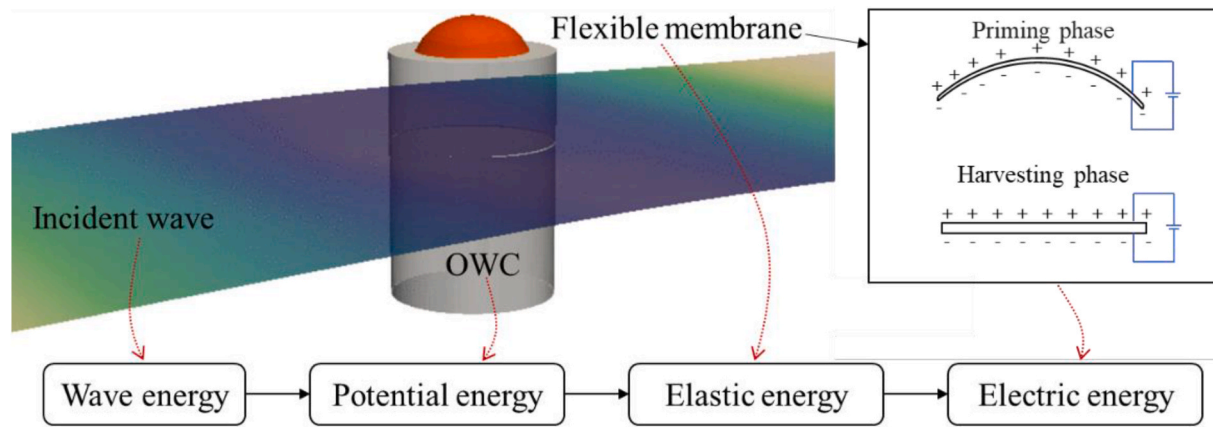
Fig. 1. Schematic diagram of energy conversion in the Novel flexible OWC.

and planar tests can be used to determine hyperelastic models [20,21]. Furthermore, the circular bulge test is an experimental procedure that can evaluate the hyperelastic model for flexible membrane. To conduct this test, a circular film or thin sheet with an initial thickness of t_0 is clamped between a fixture (or lid) and a holder. Then a fluid or gas with pressure (P) is used to inflate the membrane, and the pressure inside the holder (air chamber) and the diaphragm deformation, will be measured by using a range of sensors and image analysing method. This test has gained significant attention in recent years for its ability to accurately characterise materials [22–24], especially applications under biaxial or equi-biaxial stress conditions. Also, this method avoids the effects of friction and edge damages that may occur when the sample is clamped on the tensile machine [25,26].

To properly study the impact of membrane materials in WEC systems, conducting experiments on a water tank or dry test rig in addition to numerical and analytical analysis is necessary. Over the past few years, multiple experiments involving sea state [27], water tanks [28, 29] and dry runs [30–32] have been conducted to analyse the impact of flexible membrane materials OWCs. In order to address the high costs associated with experimental studies and the uncertainties that come with measurement equipment, a combination of numerical, analytical, and experimental approaches can be more efficient for this field.

The key novelty of this work lies in the multifaceted approach combining diverse experimental techniques and computational simulations to enable a holistic characterisation and analysis of flexible membranes for OWC WECs. While past studies have utilised individual tests or models, this integrated methodology encompasses (1) A new bulge test rig design and robust hyperelastic model selection process to characterise elastomer samples efficiently. Since the bulge test deformation mode is similar to that of the material in the OWC, it is conducted to determine the most appropriate hyperelastic model for the elastomers. (2) Real-world wave tank experiments on a scaled OWC provide simulation validation data. (3) A customised dry test rig overcoming previous pressure limitations for examining wider material options. (4) Extensive FEA parametric studies generating stress visualisations and quantifying impacts of geometrical, material and operational factors. (5) Detailed structural analyses offering new perspectives on failure risks and design optimisation strategies. By synergising multiple experiments, simulations and analyses, the approach facilitates a comprehensive evaluation of membrane mechanics to advance OWC efficiency, reliability and performance. The combined methodologies and in-depth insights promise significant contributions toward engineering sophisticated soft components for next-generation OWC wave energy systems.

2. Material characterisation process

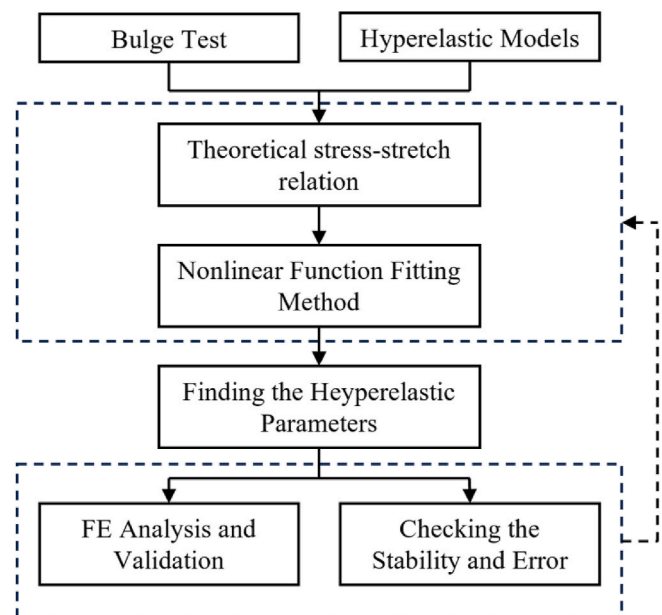The bulge test is conducted as the main procedure of the

Fig. 2. Overview of the methodology in this work.

experimental campaign considering the nature of multiaxial stress configuration. The various types of flexible membranes are tested, and the materials' properties are extracted to find proper hyperelastic models. Fig. 2 illustrates the steps outlined in this process. The stress-stretch results will be calculated from the pressure and deformation data obtained through the bulge test using the equations provided in section 2.2. After which, the results will be fitted to different hyperelastic models, and the unknown parameters will be computed beside their root mean square error (RMSE) and stability conditions. The hyperelastic models will be used alongside the numerical simulation to process the bulge test numerically, and the experimental results will justify the accuracy of the hyperelastic models. In this paper, the pressure transducer data, which represents the interaction of the elastomer membrane and airflow, is used as the loading case in the Abaqus simulation instead of running the fluid-solid interaction analysis. Finally, the most suitable models will be selected based on stability conditions, error analysis, and validation based on finite element analysis.

2.1. Experimental setup and measurement equipment

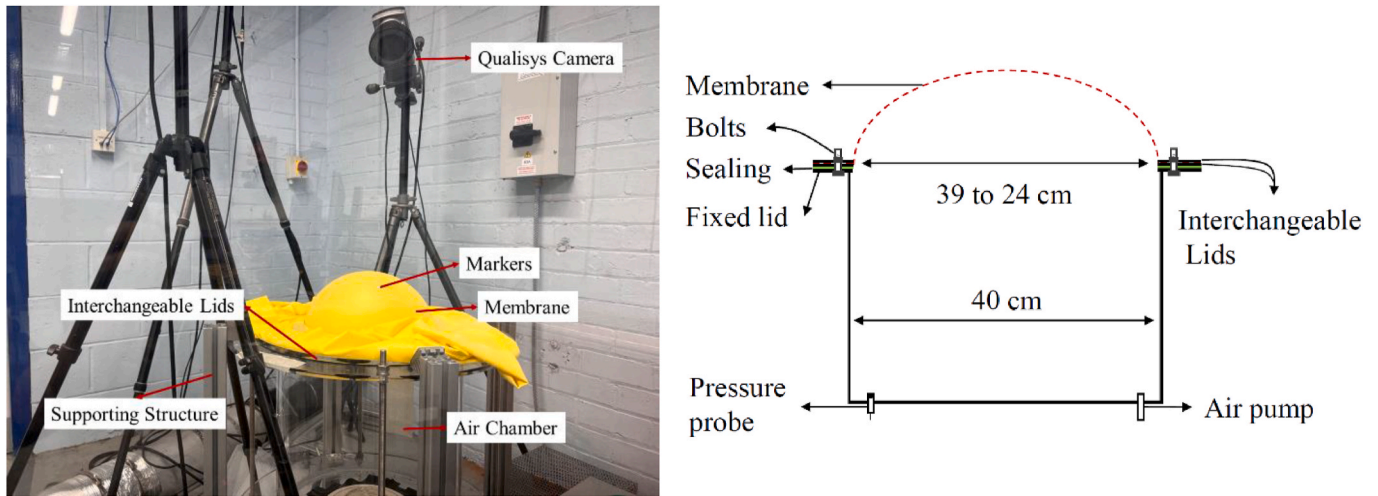Fig. 3 shows the configuration arranged for the bulge test. The setup

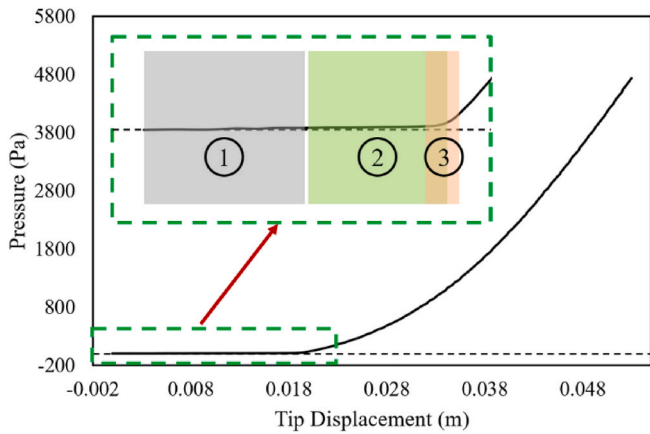**Fig. 3.** The experimental setup of the bulge test.

Fig. 4. Pressure-deformation characteristics: unprocessed data.

involves an acrylic cylinder (an air chamber) securely positioned between a supportive structure. On one end, the elastomer membrane is affixed securely to prevent any leaks, while on the opposite side, an air pump is attached to apply consistent pressure to the air chamber. The pressure inside the air chamber was raised at a steady rate of 1.8 Pa/s, resulting in a relatively low strain rate for all the samples. In the

experimental setup, we employed the Qualisys motion capture system for detailed measurements of elastomer deformation. This system utilises infrared light and specific markers attached to the membrane, and its functionality is augmented by three high-resolution cameras (Qualisys Oqus 300+) positioned above the cylinder. The Qualisys system was crucial in capturing precise data, ensuring a thorough examination of membrane behaviour during the experiments. During testing, a Honeywell SDX01G2 pressure transducer with a maximum reading range of 1 psi is connected to the cylinder to measure the pressure inside the air chamber. The pressure transducer is connected to data acquisition equipment (CED1401 Micro 3, produced by Cambridge Electronic Design Limited), and generated results are processed by Spike2, an acquisition system software provided by the same company. Experiments on membranes with various diameters, up to 39 cm, can be accommodated by adjusting the setup lid. Two key considerations justify the choice of a 24 cm diameter lid for the bulge test and characterisation process. The first reason is the maximum range of the available pressure transducer, which determines the upper limit of the readings. The second reason is that samples need to be characterised within their deformation range for applications in OWC. After conducting different experiments using various lid diameters, we have found that the 24 cm lid diameter fulfils all requirements.

Fig. 4 illustrates the experimental pressure-deformation data that has not been processed. The figure highlights three phases associated with the inverse deformation, not-fully-bent, and starting states. Before
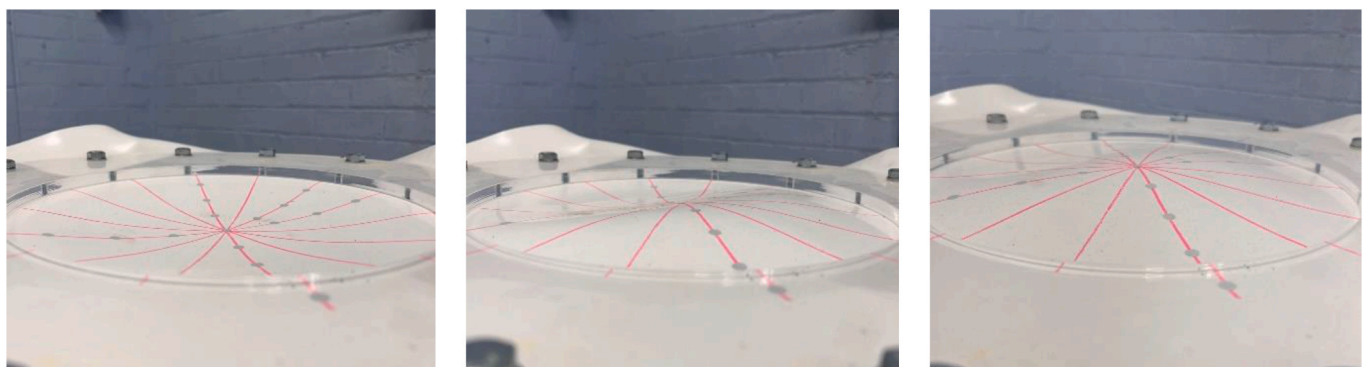
a) Inverse deformation state   **b) Not-fully-bent state**   **c) Starting the data processing**

Fig. 5. Comparison of the sample in three different kinematic states.

conducting each test, the air chamber's end is opened to balance the pressure inside and outside. This ensures that no pressure differential exists initially on the membrane. In this state, the membrane diaphragm undergoes inverse deformation (phase 1) due to the weight of the material, as illustrated in Fig. 5-a. As pressure increases, the sample undergoes non-uniform deformation (phase 2) without membrane stretching, as shown in Fig. 5-b. Characterising the samples from these states will lead to a less stiff hyperelastic model, given that even a slight pressure induces deformation. The accuracy of the bulge test results depends significantly on the initial condition of the membrane. This intricacy has been extensively studied by Small and Nix [33] and Jackson [34]. This study assumes main zero stress-stretch conditions after a specific amount of centre deformation (tip displacement) to ensure consistent results and minimise errors in the characterisation process. The determination of this state is a multistep process guided by a thorough examination of the samples' appearance, the trend of the pressure-deformation curve, and a trial-and-error procedure. As mentioned, the unpressurised membrane exhibits pre-deformation from its weight, and as pressure is gradually increased, we evaluate the membrane's appearance. We incrementally increase pressure inside the air chamber, visually confirming the disappearance of the not-fully-bent state. Phase 3 involves a trial-and-error approach to refine and select the starting point of data processing. It begins with characterising elastomer membranes and concludes by verifying the stability and accuracy of hyperelastic models. During Phase 3, we included the not-fully bent state before its complete disappearance to consider all critical experimental data in the characterisation process (see Fig. 4 for details). These adjustments are made to ensure a reliable and robust characterisation process for the full range of evaluated deformations.

2.2. Theoretical formulation

This section builds the foundation by deriving equations that connect the experimental pressure-deformation data to the stress-stretch relationship. Throughout the experiment, we measured the membrane's tip displacement using the Qualisys system and tracked the air chamber pressure with a pressure transducer. In the conducted bulge test, the axisymmetric nature of the geometry, loading, and boundary conditions allow for considering equibiaxial conditions in the equations [35]:

$$\lambda_1 = \lambda_2 = \lambda, \qquad \lambda_3 = \lambda^{-2}$$
$$\sigma_1 = \sigma_2 = \sigma, \qquad \sigma_3 = 0 \tag{1}$$

where σ_i ($i = 1, 2$ and 3) and λ_i ($i = 1, 2$ and 3) are principal stresses and stretches. The stress-stretch results are calculated from the following equation [34]:

$$\sigma = \frac{P\left[a^2 + (h_0 + h)^2\right]}{4(h_0 + h)t} \tag{2}$$

In which P is pressure inside the air chamber, a is the primary radius of the elastomer, h is the deformation of the centre (tip displacement), t is the elastomer thickness, and h_0 is the tip displacement in the zero stress-stretch states. The calculation of h_0 to be 1 cm was carried out in this paper using the process discussed in the previous section. The stretch (λ) is calculated as the ratio of the deformed length (s_1) to the initial length (s_0) as following relation [34,36]:

$$\lambda = \frac{s_1}{s_0} \tag{3}$$

where the initial and deformed length of the membrane in the r-direction can be determined as [34]:

$$s_0 = \frac{a^2 + h_0^2}{h_0} \sin^{-1}\left(\frac{2ah_0}{a^2 + h_0^2}\right) \tag{4}$$

and

$$s_1 = \frac{a^2 + (h_0 + h)^2}{(h_0 + h)} \sin^{-1}\left(\frac{2a(h_0 + h)}{a^2 + (h_0 + h)^2}\right) \tag{5}$$

By multiplying the stress and stretch, the true (Cauchy) stress, T, can be obtained:

$$T = \sigma\lambda \tag{6}$$

2.3. Hyperelastic models

Based on the material's intrinsic properties, hyperelastic constitutive models establish a correlation between stress and strain conditions. This section presents the stress-stretch relationship of various hyperelastic models to be used in the curve-fitting process. Selecting an accurate hyperelastic model is crucial to ensure precise predictions and align the mathematical representation with the actual structure's behaviour. This is especially important in predicting the behaviour of flexible membranes when they undergo large deformations. Hyperelastic models are usually defined in a strain-energy function (W) form. Since we assumed that samples are ideally elastic (under isothermal and adiabatic conditions), isotropic and incompressible, W can be defined as a function of the principal stretches ($W(\lambda_1, \lambda_2)$). Also, it is common to write the hyperelastic models as a function of strain invariants, denoted as I_i ($i = 1,2$ and 3), which are a function of principal stretches as follows [37]:

$$I_1 = \lambda_1^2 + \lambda_2^2 + \lambda_3^2$$
$$I_2 = (\lambda_1\lambda_2)^2 + (\lambda_1\lambda_3)^2 + (\lambda_2\lambda_3)^2 \tag{7}$$
$$I_3 = (\lambda_1\lambda_2\lambda_3)^2$$

Where, for the incompressible condition I_3=1. Substituting Eq. (1) into Eq. (7) yields the following strain invariants for equibiaxial conditions:

$$I_1 = 2\lambda^2 + \lambda^{-4}$$
$$I_2 = 2\lambda^{-2} + \lambda^4 \tag{8}$$

The stress-strain relationship for various elastomers, particularly under biaxial loading conditions, is inaccurately described by classic hyperelastic models like the Neo-Hookean model [38]. In this study, we analyse and characterise the samples using five commonly used hyperelastic models: first-order Moony-Rivlin (FOMR), second-order Moony-Rivlin (SOMR), Yeoh, Ogden with $N = 3$, and Arruda-Boyce (AB).

2.3.1. Polynomial form of hyperelastic model

The Mooney-Rivlin model is a popular hyperelastic model used to describe the nonlinear elastic behaviour of rubber-like materials. It allows for accurate predictions of mechanical responses under various loading conditions, such as compression, tension, and shear. This model compensates for the shortcomings of the Neo-Hookean model by including a dependence on the second invariant. Equation (9) represents the polynomial form of the strain energy function [14,39]:

$$W = \sum_{i+j=1}^{N} C_{ij} (I_1 - 3)^i (I_2 - 3)^j \tag{9}$$

In equation (9), the strain energy functions for the FOMR and SOMR models can be derived when N equals 1 or 2, respectively.

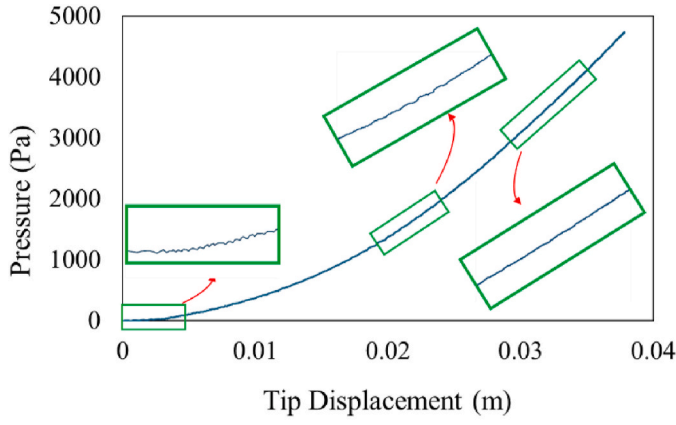FOMR model:

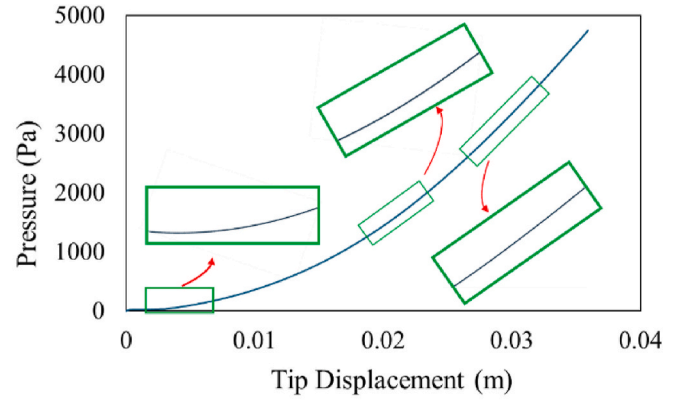$$W = C_{10} (\bar{I}_1 - 3) + C_{01} (\bar{I}_2 - 3) \tag{10}$$

SOMR model:

$$W = C_{10} (\bar{I}_1 - 3) + C_{01} (\bar{I}_2 - 3) + C_{20} (\bar{I}_1 - 3)^2 + C_{11} (\bar{I}_1 - 3)(\bar{I}_2 - 3) + C_{02} (\bar{I}_2 - 3)^2 \tag{11}$$
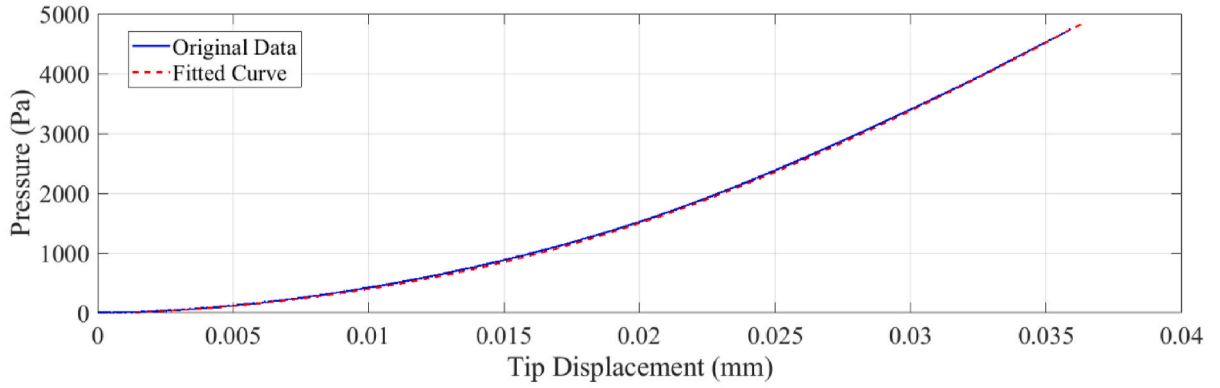
In which C_{ij} are constants parameters of the materials and can be determined by the experimental data. The principal Cauchy stress can be achieved using the following equation:

a) Original noisy data

b) 7th-order Polynomial Fitted Curve

c) Comparative Insight into Noise Reduction Strategies

Fig. 6. Exploration of data refinement.

$$T = \lambda \frac{\partial W}{\partial \lambda} \tag{12}$$

Substituting Eqs. (10) and (11) and Eq. (7) into Eq. (12) leads to the stress function in equibiaxial condition for the FOMR and SOMR models:

FOMR model:

$$T = 2(\lambda^2 - \lambda^{-4})[C_{10} - C_{01}\lambda^2] \tag{13}$$

SOMR model:

$$T = 2(\lambda^2 - \lambda^{-4})[C_{10} - C_{01}\lambda^2 + 2C_{20}(\bar{I}_1 - 3) + C_{11}(\lambda^2(\bar{I}_1 - 3) + (\bar{I}_2 - 3)) + 2C_{02}\lambda^2(\bar{I}_2 - 3)] \tag{14}$$

2.3.2. Ogden model

Another well-known form of the hyperelastic model is proposed by Ogden [15,40,41]:

$$W = \sum_{i=1}^{N} \frac{2\mu_i}{\alpha_i^2}(\lambda_1^{-\alpha_i} + \lambda_2^{-\alpha_i} + \lambda_3^{-\alpha_i}) \tag{15}$$

The constants parameters of materials, μ_i and α_i, can be determined through experimental data. Substituting Eq. (15) into Eq. (12) under equibiaxial conditions results in the following stress [42]:

$$T = \sum_{i=1}^{N} \frac{2\mu_i}{\alpha_i}(\lambda^{\alpha_i} - \lambda^{-2\alpha_i}) \tag{16}$$

There is no limitation on the value of N; however, the $N = 3$ condition, which is widely employed in different studies [43–45], is also used in this paper.

2.3.3. Yeoh model

The strain energy potential and stress function of the Yeoh hyperelastic model, which can be generated by the reduced polynomial strain energy potential function with $N = 3$, is as follow [46]:

$$W = C_{10}(I_1 - 3) + C_{20}(I_1 - 3)^2 + C_{30}(I_1 - 3)^3 \tag{17}$$

$$T = 2(\lambda^2 - \lambda^{-4})(C_{10} + 2C_{20}(I_1 - 3) + 3C_{30}(I_1 - 3)^2) \tag{18}$$

In which (C_{i0} $i = 1$, 2 and 3) are the material parameters that can be achieved with the experimental data and curve fitting process.

2.3.4. Arruda–Boyce (AB) model

Arruda-Boyce is another hyperelastic model used by many researchers [47–50]. The strain energy and stress function of the AB hyperelastic model is as follows:

$$W = \mu \sum_{i=1}^{5} \frac{C_i}{\lambda_m^{2i-2}}(I_1^i - 3^i) \tag{19}$$

$$T = 2\mu(\lambda^2 - \lambda^{-4}) \sum_{i=1}^{5} \frac{iC_i}{\lambda_m^{2i-2}} I_1^{i-1} \tag{20}$$
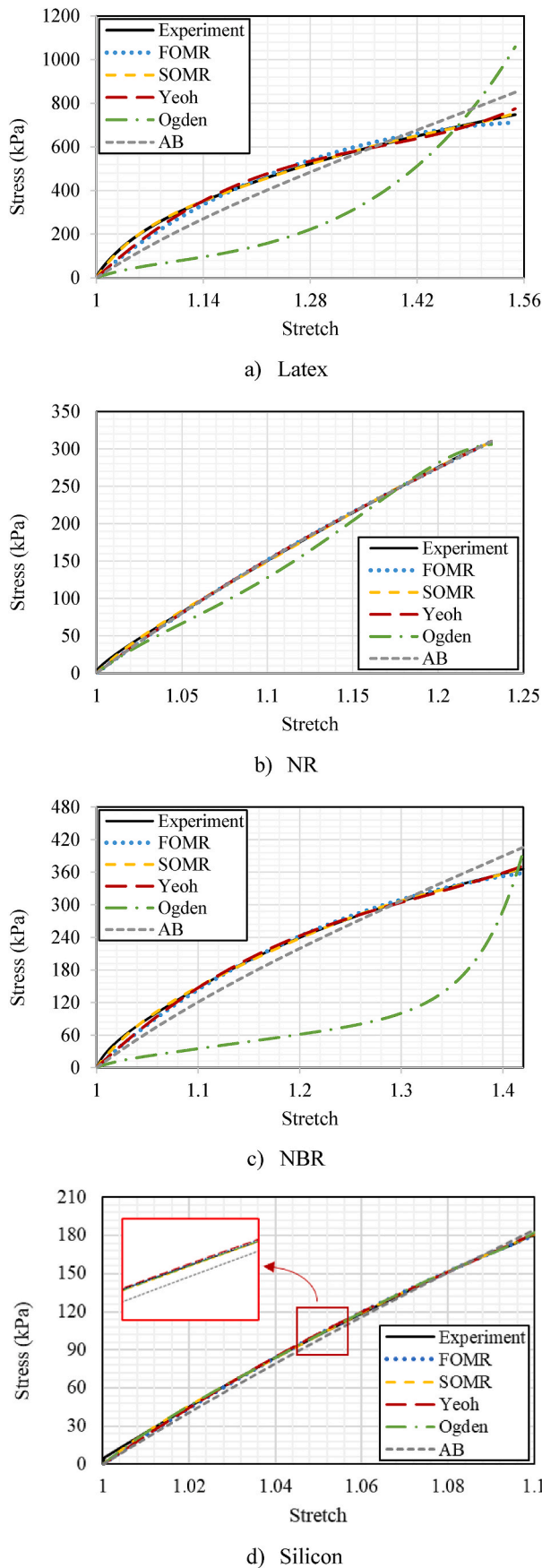
Fig. 7. Comparison of stress-stretch behaviour between experimental results and fitted models for a) latex, b) Natural Rubber, c) NBR, and d) silicon.

Table 1

Hyperelastic parameters obtained from curve fitting of experimental data from the bulge test for latex, NR, NBR and silicon.

Model	Parameters	Material			
		Latex	NR	NBR	Silicon
FOMR	C_{10} (MPa)	0.3280	0.1448	0.1892	0.3051
	C_{01} (MPa)	−0.0701	−0.0095	−0.0436	−0.1107
	Stability	<0.6	<7.7	<0.55	<0.32
	RMSE (MPa)	0.0234	0.0021	0.0059	0.0011
SOMR	C_{10} (MPa)	1.4956	0.7466	0.7607	1.6991
	C_{01} (MPa)	−1.0796	−0.5639	−0.5565	−1.4624
	C_{20} (MPa)	0.7345	1.8860	0.6791	42.095
	C_{11} (MPa)	−0.3616	−2.0101	−0.5121	−66.303
	C_{02} (MPa)	0.0798	0.6164	0.1329	26.81
	Stability	<1.73	<0.68	<1.12	<0.25
	RMSE (MPa)	0.00297	0.0010	0.0020	0.00069
Ogden ($N = 3$)	μ_1 (MPa)	0.5758	0.0233	−0.0689	0.0071
	α_1	−4.6303	−12.9629	−14.8772	−41.5455
	μ_2 (MPa)	−0.6756	−0.0635	0.1377	0.4955
	α_2	−4.6021	−11.8209	29.7563	21.3255
	μ_3 (MPa)	0.3082	0.3403	0.0620	−0.0293
	α_3	8.7376	14.7055	1.9461	−24.7779
	Stability	Stable	<0.24	Stable	<1.03
	RMSE (MPa)	0.2156	0.0117	0.1471	0.00083
Yeoh	C_{10} (MPa)	0.2689	0.1442	0.1456	0.1924
	C_{20} (MPa)	−0.0546	−0.0028	−0.0299	−0.1818
	C_{30} (MPa)	0.0103	0.0030	0.0073	0.5402
	Stability	Stable	Stable	Stable	Stable
	RMSE (MPa)	0.0179	0.0021	0.0053	0.0011
AB	μ (MPa)	0.3823	0.2868	0.2292	0.3503
	λ_m ($\times 10^5$)	−3.2471	1.0964	4.7455	0.0725
	Stability	Stable	Stable	Stable	Stable
	RMSE (MPa)	0.0604	0.0021	0.0212	0.0032

where μ and λ_m are the constant parameters which can be calculated by using experimental data. Also, the C_i constants are as follows:

$$C_1 = \frac{1}{2}, C_2 = \frac{1}{20}, C_3 = \frac{11}{1050}, C_4 = \frac{19}{7000}, C_5 = \frac{519}{673750} \quad (21)$$

2.4. Experimental results and model fitting

This section uses the bulge test experimental results to fit several hyperelastic models, including the FOMR, SOMR, Yeoh, Ogden ($N = 3$), and AB models. The chosen materials are commonly used in laboratories or large-scale experiments on OWC WECs, including silicon (3 mm thickness), NR (1.5 mm thickness), NBR (1 mm thickness), and latex (0.2 mm thickness). The membranes experienced reasonable strain levels for the OWC-WEC. Characterising elastomers at extensive strains is avoided as it could unrealistically change the membrane properties for the intended application. The bulge test was conducted on three samples of each material to ensure the results. Each diaphragm sample was subjected to preloading through multiple deformations before the primary characterisation test. This process leads to a more consistent stress-strain response and minimises transient effects. A preprocessing step was conducted to enhance experimental data quality, specifically focusing on pressure transducer data. The goal was noise removal while retaining crucial data for subsequent analysis. Notably, characterising samples with noisy experimental results can reduce the stability range of hyperelastic models. In this step, a 7th-order polynomial was fitted to the experimental results instead of using methods, such as using smooth
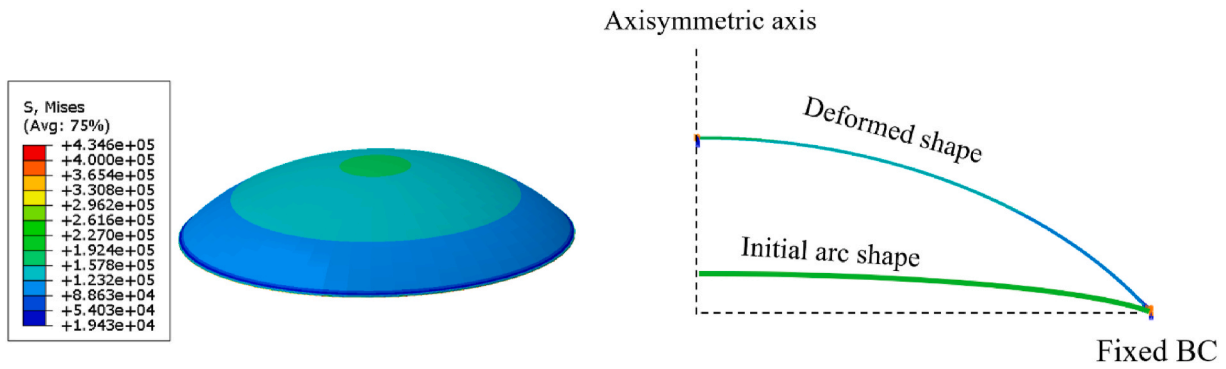
Fig. 8. Abaqus simulation and swept view of the result.

function, that could alter the curve's intrinsic features. Fig. 6-a illustrates the original data with noise, while Fig. 6-b displays the fitted curve after noise removal. Fig. 6-c presents both plots together for comparison.

After applying the noise removal process, the pressure-deformation data were converted into stress-stretch results, utilising the equations provided in section 2.2. Next, the stress-stretch data were fitted to different hyperelastic models using MATLAB's lsqcurvefit function. This function, which is an iterative optimisation algorithm, works based on minimising the sum of squared residuals and adjusting the defined function's unknown parameters that best fit a given set of data. Fig. 7 (a–d) show different hyperelastic models fitted to the bulge test results of the mentioned materials.

Furthermore, Table 1 shows the hyperelastic parameters of different models for tested materials, the stability of models (using the Drucker stability condition [51]) and the RMSE between the stress-stretch of experimental results and fitted curves.

When selecting the best hyperelastic models for a material, it is crucial to consider both stability and RMSE of the models. The AB hyperelastic model, for example, is guaranteed to be stable if the shear modulus and locking stretch have positive values; however, its RMSE should also be considered when deciding which model to use. In the next step, to validate the generated hyperelastic models and the bulge test data, the hyperelastic model data were used as input in the computational software (Abaqus) for the material property, and the conducted experiment was simulated.

2.5. Numerical simulation and validation

As previously outlined, numerical validation is another critical phase in selecting the hyperelastic model. Abaqus is used to simulate the bulge test, and the calculated deformation of the elastomers was verified with data from Qualisys's system. In Section 2.1, we underscored that the weight of the samples induces a non-flat primary shape, necessitating consideration of an initial arc configuration. Accurate numerical simulation requires addressing this non-flat state, especially given the assumption of zero stress in this condition. This consideration becomes essential when directly comparing simulated data with the experimental results obtained from the Qualisys system. To integrate the arc shape into the numerical simulation, the arc radius is introduced using the following equation:

$$R = \frac{a^2 + (h_0 + h)^2}{2(h_0 + h)} \qquad (22$$

Fig. 8 illustrates the stress results of the NBR using the SOMR hyperelastic model. This simulation utilises the 4-node bilinear axisymmetric quadrilateral element (CAX4H), which is well-suited for capturing large deformations in axisymmetric conditions. One end of the elastomer part is clamped, while the left end, which represents the centre of the elastomer, is assumed to have an axisymmetric boundary

condition, as shown in Fig. 7. The nonlinear geometry (NLGEOM) option is used to analyse the large deformation accurately. Pressure transducer data, representing fluid-solid interaction in actual conditions, is applied as a loading state on its surface to simulate the elastomer membrane's behaviour.

Fig. 9(a–d) compare pressure against the tip displacement between the numerical simulation and experimental results. The fact that the simulations and experiments match well indicates that the generated models can accurately predict the material's behaviour.

2.6. Results and discussions

In the following, the discussion for each material and the most suitable hyperelastic model is provided:

Latex:

Table 1 shows that although the Ogden model is stable, it has a high RMSE, which can be seen in Fig. 7-a. According to Table 1, the SOMR gives a better fitting with an RMSE of 0.00297 MPa. Although this model is unstable for biaxial tension at a nominal strain higher than 1.73, we will use this model in the next section since the observed deformation is in the range of the model stability. Also, the Yeoh model, which is stable and has a relatively low RMSE, would be a better option for extreme deformation analysis. Furthermore, Fig. 9-a, which compares the Abaqus simulation with different hyperelastic models with the bulge test results, shows that the results of the Ogden and AB models have a high discrepancy with the experimental results.

NR:

According to Table 1, the SOMR, which is stable for nominal strain less than 0.68, has a lower RMSE than other models. However, FOMR, Yeoh and AB also have good stability and low RMSE for extensive deformation analysis. From Fig. 9-b, it is evident that all the generated hyperelastic models can accurately predict the deformation of the NR. This is likely due to the NR sample having a greater thickness than the latex sample, resulting in more consistent outcomes and stable hyperelastic models.

NBR:

For the NBR, the SOMR with the RMSE of 0.002 MPa gives better fitting than other models with experimental results. Since this model is stable for nominal strain less than 1.12, FOMR and Yeoh hyperelastic models can be used for more extensive deformation analyses. Based on Fig. 9-c, both the Ogden and AB models have a high error level when predicting sample deformation, with RMSE values of 0.1471 MPa and 0.0212 MPa, respectively. However, as mentioned, the SOMR, FOMR and Yeoh models are suitable for conducting numerical simulations on NBR.

Silicon:

In the case of silicon, almost all the hyperelastic models have a relatively low RMSE, ranging from 0.00069 MPa to 0.0032 MPa at most. Regarding stability parameters, the AB and Yeoh models are suitable for analysing large deformations, while the Ogden model is best for nominal
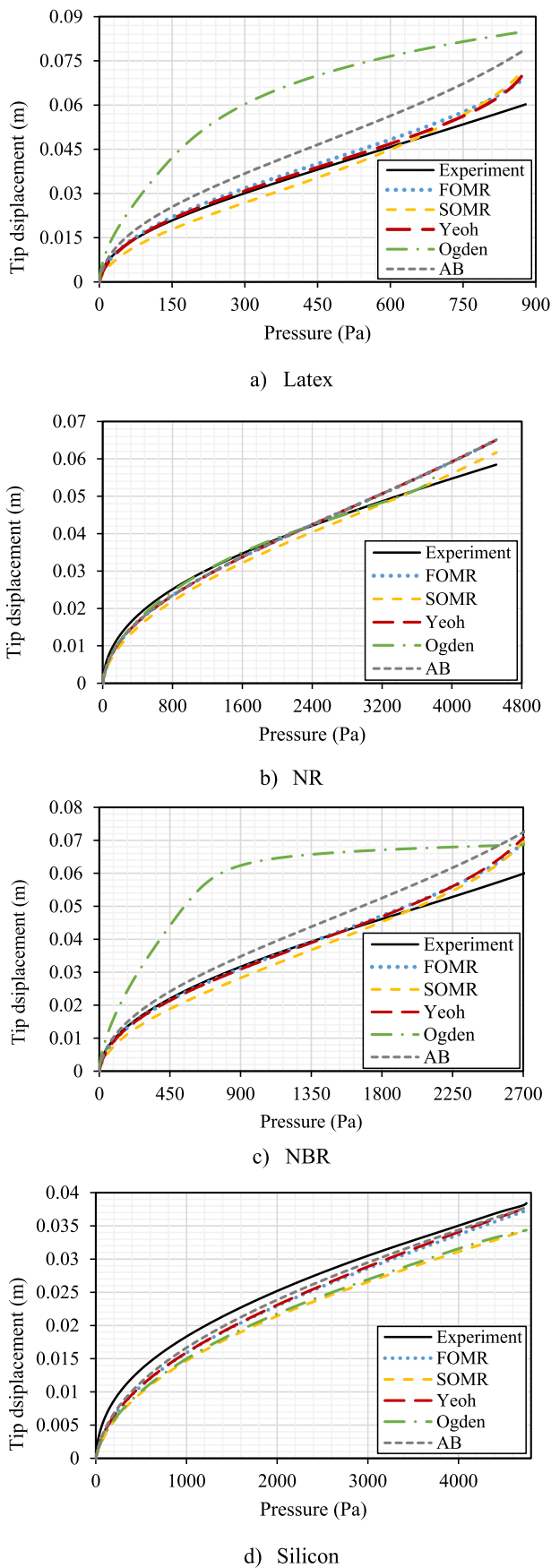
a) Latex

b) NR

c) NBR

d) Silicon

Fig. 9. A comparison between displacement (m) and pressure (Pa) for experimental and Abaqus numerical data.

strains below 1.03. Also, it can be seen from Fig. 9-d that all the generated hyperelastic models can adequately predict the behaviour of the silicon. The same conclusion was observed for the NR, which shows that the accuracy of this characterisation method depends on the aspect ratio (the ratio between the diameter per thickness) of elastomers.

3. Water tank test

3.1. Experimental setup and equipment

The experiments were conducted at the Kelvin Hydrodynamic Laboratory (KHL) of the University of Strathclyde (UK) using a 3D compact wave tank measuring $9.575 \times 3.150 \times 1.000$ m. This tank can generate waves within a 0.5–5 s period and reach a maximum wave height of 0.3 m. Considering the tank's specifications, a small-scale OWC model was considered for the prototype, as depicted in Fig. 10, with a scale factor ranging from 1:30 to 1:20, based on the Froude scaling criteria [57]. The setup consisted of an acrylic cylinder and two top discs for fixing the elastomer at the top. A specially designed fixture, created via a three-dimensional (3D) printing process, affixed the device to the supporting structure.

The wave amplitude and frequency effect on the membrane was examined by generating various waves using wave generator software. The accuracy of wave conditions was assessed by data obtained from the reference point (RP) wave probe positioned 2 m away from the cylinder. Also, another wave probe, the OWC wave probe, is used inside the cylinder to measure the wave elevation inside the air chamber during the test. The wave probes, manufactured by KHL, comprised two parallel rods. One end of the wave probe was connected to the data acquisition equipment, while the other end extended below the water surface. Changing the water level between the rods leads to variations in resistance and voltage. Also, the Qualisys system and a pressure transducer (Honeywell 163PC01D75) with ± 2.5 inches of water gauge (in wg) were used to measure the membrane's deformation and the pressure inside the air chamber during the experiment.

3.2. Tank test results

This section presents the tank test's experimental results on the OWC with the membrane part. Due to the pressure limitation inside the air chamber, latex is used as the flexible membrane in this experiment to have enough deformation. The first step was generating a particular wave condition (with an amplitude of 0.01 m and frequency of 0.4 Hz), which led to the pressure transducer data, Fig. 11. These data were employed as the loading condition for the numerical simulation to cross-verify the results with those obtained from the Qualisys system. Each trial lasted 180 s, and the steady results are illustrated in the plotted graphs and used in the numerical simulations. Fig. 12 shows that the results of the FE simulation with Yeoh and SOMR hyperelastic models are in excellent agreement with those of the experiments. The discrepancy between the numerical and experimental simulation can be due to the uncertainty of the measurement equipment.

In the following, three particular cases are considered for the experiment: Open-top (OWC without a lid), rigid-top (OWC with a rigid lid) and latex (OWC with a latex layer at the top). This experiment is conducted to study the effect of the elastomer part on the OWC's performance, where the open-top case represents a case without a PTO system and leads to the maximum elevation response of the OWC. On the other hand, the rigid-top condition represents an over-damped scenario which provides the maximum possible pressure response inside the chamber. The above two test conditions indicate the practical maximum response of the elevation and the maximum pressure response of the current OWC device. Fig. 13 illustrates the pressure inside the air chamber for three cases, and as expected, the pressure amplitude for the case of latex is between those of Open and Rigid-top cases.

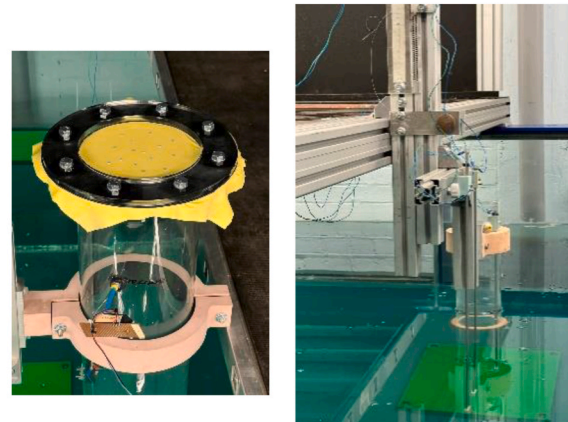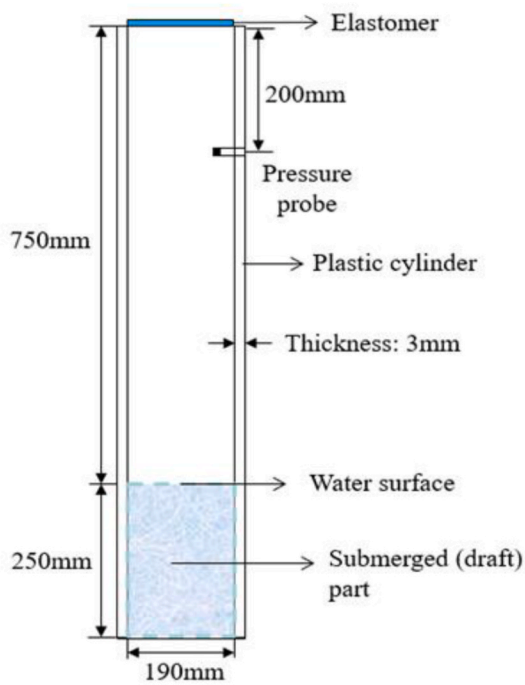Fig. 14 shows the response amplitude operator (RAO), the ratio of

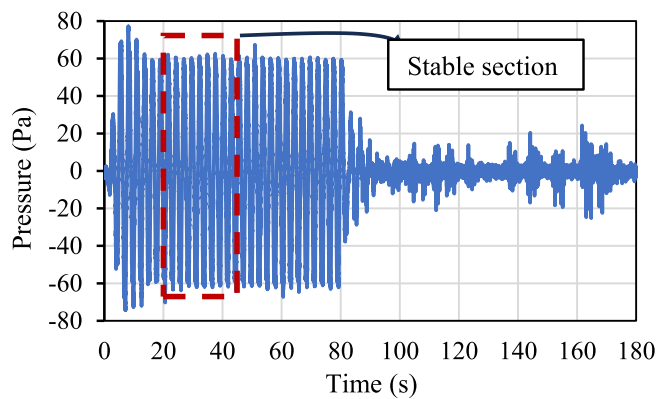**Fig. 10.** Geometrical Specifications and Experimental Setup of the OWC at the water tank.

Fig. 11. The pressure inside the air chamber for the wave with an amplitude of 0.01m and frequency of 0.4 Hz.
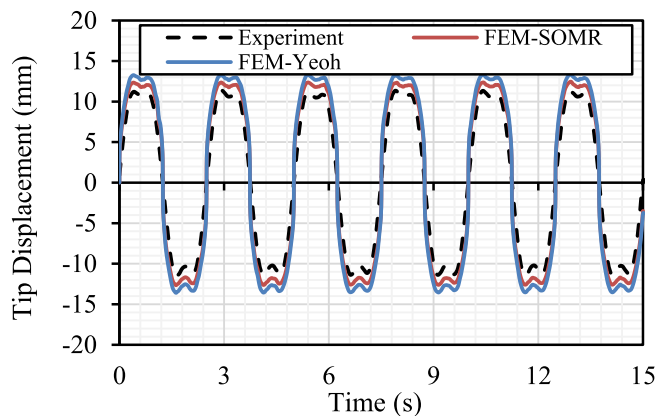

Fig. 12. Experimental and numerical results of tip displacement versus time.

the water elevation inside the air chamber (OWC wave probe data) per wave height (RP wave probe data), as a function of the frequency for the three mentioned cases. The figure is generated by conducting a series of tests with a fixed wave amplitude of 0.01 m and different frequencies, ranging from 0.25 Hz to 1.4 Hz, with an increment of 0.05 Hz in each trial. Based on the frequency response analysis, it is evident that the OWC with a membrane has a smoother fluctuation without any spikes. This feature can be advantageous for WECs as, in actual sea conditions, the waves are unpredictable, and utilising membranes or DEGs can lead to consistent power outputs.

Also, the RAO versus wave amplitude for the latex material is plotted in Fig. 15 and shows that increasing the wave amplitude can reduce the RAO and, consequently, the deformation and power generation. This chart was created by performing multiple tests using a consistent wave frequency of 0.375 Hz but varying wave amplitudes between 3 mm and 24 mm.

4. Dry test rig experiment

4.1. Test rig setup and equipment

During the water tank test, using elastomer membranes with higher thicknesses was not recommended due to the low pressure inside the air chamber. A dedicated dry test rig was designed and fabricated, Fig. 16, to overcome this limitation and further explore the influence of different parameters on the flexible membrane used in OWC-WEC. This custom rig simulates the deformation of the elastomer diaphragm in OWC and allows for comprehensive investigations into the materials and structural solutions to enhance the OWC's efficiency and reliability. A brushless linear servo motor (specifically, the MOOG company's model 50206012F-LCE-CV) was employed to apply harmonic loading on the piston section with different frequencies and strokes. Within the test rig, the extent of the actuator stroke alters the pressure in the air chamber and causes deformation in the membrane portion. The same pressure transducer and Qualisys system employed in bulge tests are used to measure the pressure inside the air chamber and the deformation of the flexible component.
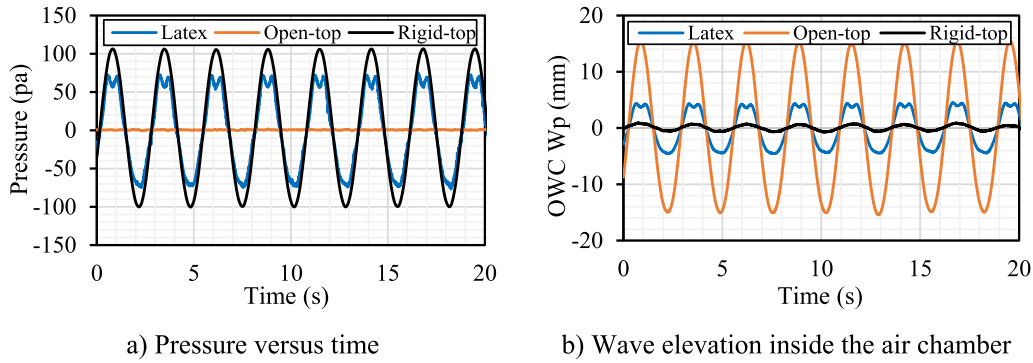
a) Pressure versus time   b) Wave elevation inside the air chamber

Fig. 13. a) Pressure and b) wave elevation inside the air chamber for the Open-top, Rigid-top, and latex cases.
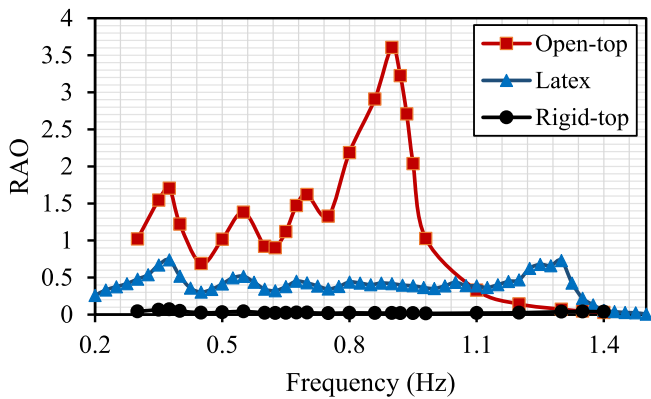

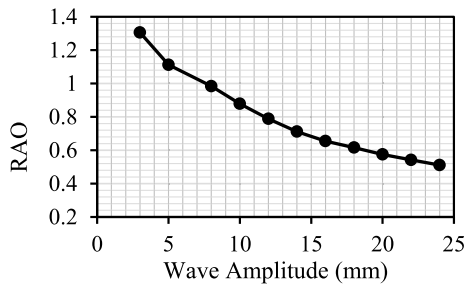**Fig. 14.** Frequency response of the latex, Open and Rigid-top cases.

Fig. 15. RAO of the OWC with latex for different wave amplitudes.

4.2. Stress analysis of inflatable diaphragm

At first, two experiments with a stroke frequency of 0.7 Hz were conducted on latex and NBR to verify the numerical results and generated hyperelastic models. Fig. 17 show the pressure inside the air chamber and tip displacement versus time for latex and NBR. It can be seen that the numerical simulation results are in excellent agreement with those of the experiments. The Abaqus results show a slight fluctuation close to the zero-deformation reference line. Although there are no visible fluctuations in the Qualisys data, using pressure transducer data as loading conditions in Abaqus simulations is responsible for the observed fluctuations. The pressure transducer's high sensitivity captures these fluctuations more prominently, highlighting their impact on the results. These fluctuations cause difficulties for DEG's energy generation process, and therefore, it is necessary to include a pre-stretching on the elastomer membranes.

Fig. 18 displays the principal stress distribution along the radial direction of the latex and NBR in their maximum deformation condition. It
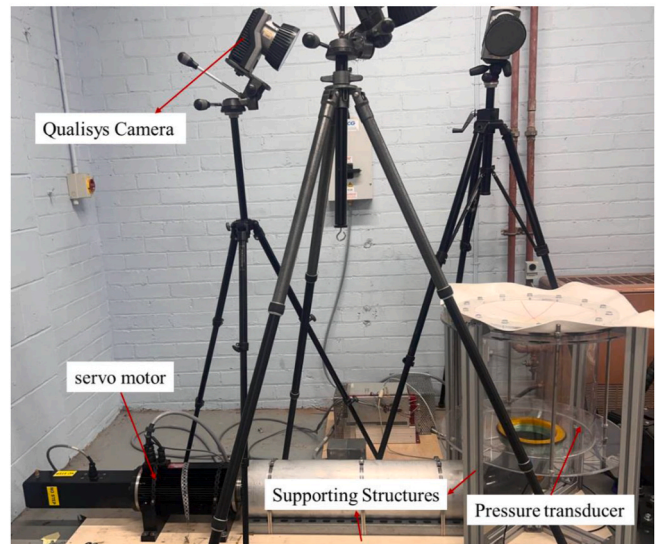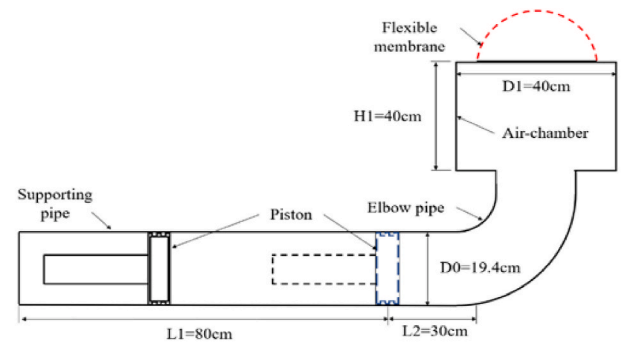

Fig. 16. The schematic diagram of the designed dry test rig.

should be noted that this figure illustrates the stress profile from the centre to the outer edge of the inflatable diaphragm. It is essential to consider that both samples' maximum stress happens at the elastomers' boundaries, particularly for fatigue analysis. Since OWC faces cyclic loading in the sea environment, tearing elastomers close to the edges with the highest stress value is one of the main failure mechanisms in this structure.

Figs. 19 and 20 present numerical simulation results that study the impact of elastomer stiffness on deformation and stress distribution. The simulations were performed on a membrane with a 24 cm diameter and 0.18 mm thickness, which was subjected to cyclic loadings at a frequency of 0.7 Hz. The simulation is repeated for NBR, latex, silicon and NR. It is evident from the figure that silicon shows the highest stiffness,
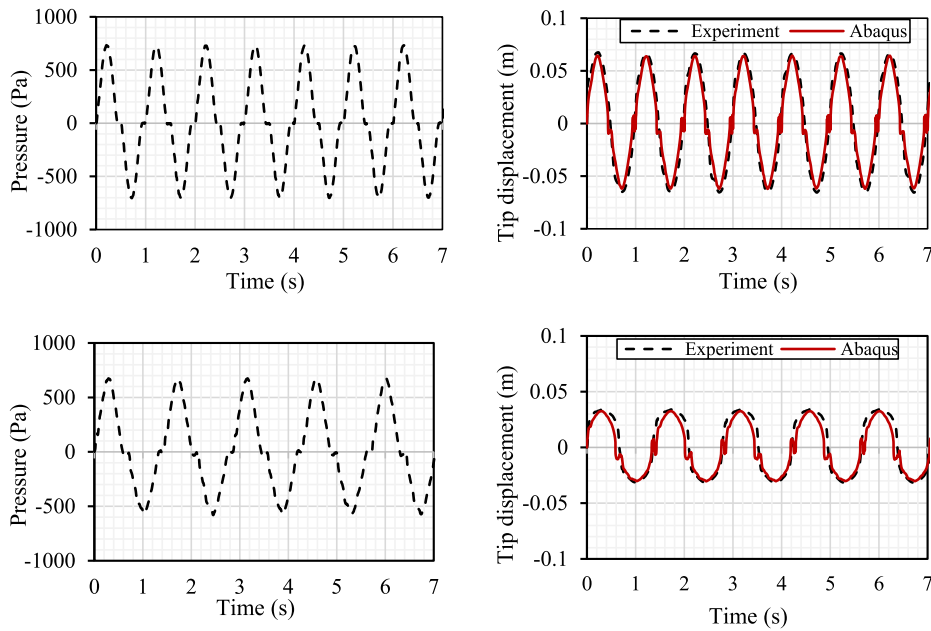
Fig. 17. Left) The pressure inside the air chamber and right) tip displacement versus time of top) latex and bottom) NBR.
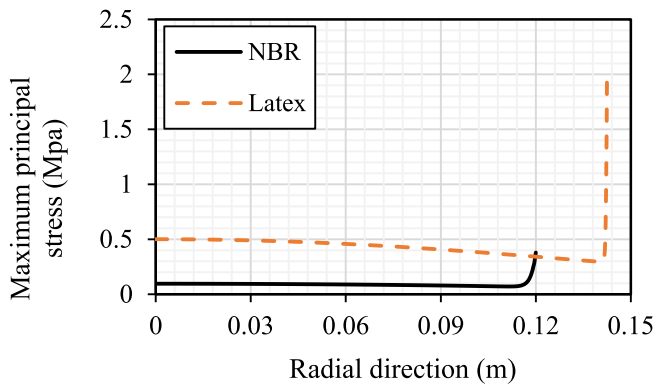

Fig. 18. The stress distribution along the radial direction of the elastomer on the maximum deformation condition.
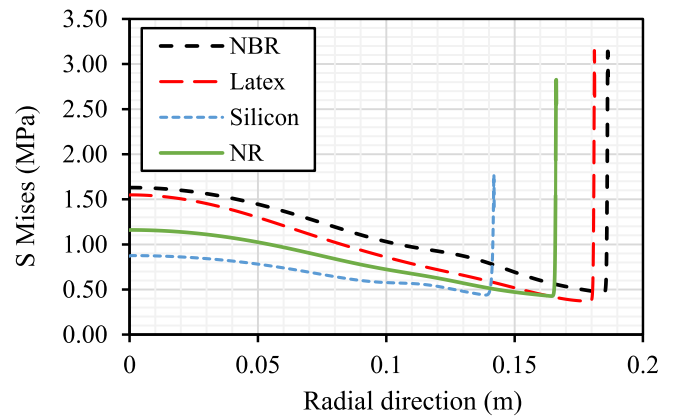

Fig. 20. The stress distribution along the radial direction of different materials on the maximum deformation condition.
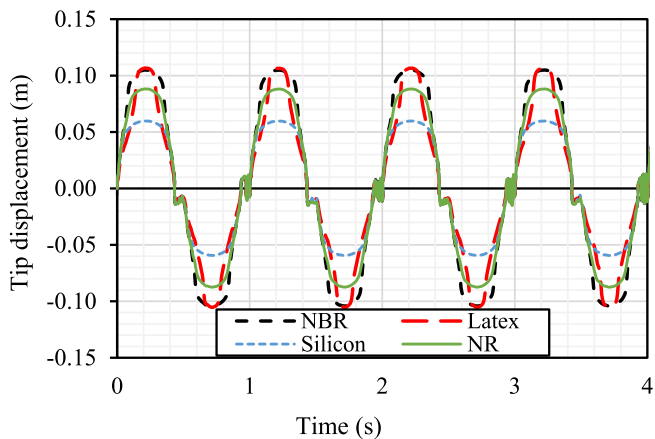

Fig. 19. Tip displacement versus time for different materials.
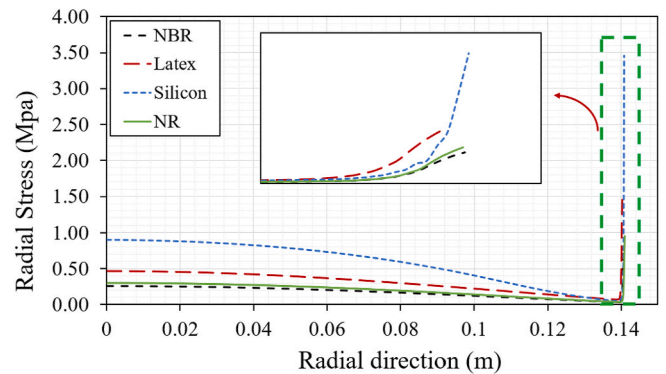
Fig. 21. The radial stress distribution along the radial direction of different materials with a same tip displacement.

followed by NR, latex, and NBR, which display relatively lower stiffness values, respectively. The material's flexibility is one of the essential parameters to consider when choosing the best material for the inflatable membrane part of the OWC. More flexibility leads to more deformation with the same wave condition and, consequently, more power generation. Also, Fig. 20 shows the stress distribution along the

radial direction of different materials on their maximum deformation condition. It is apparent that latex and NBR experience higher stress near the boundary condition. However, their stress analyses are not comparable due to different material deformation.

Fig. 21 shows the radial stress distribution along each elastomer's radial direction, with a constant tip displacement of 6 cm. The results indicate that silicon, latex, and NR have higher stress levels than NBR, with percentages of 324%, 81%, and 16%, respectively.

The proposed methodology correlates the mechanical response of flexible membranes in experimental setups with mathematical and computational modelling. However, making a solid decision to select a flexible membrane used in OWC requires considering other material selection criteria such as fatigue strength, rapture stretch, density and electrical breakdown. Meeting the objectives of the current research study to develop experimental and numerical tools and utilise them to address a series of inflatable membrane materials resulted in a more comprehensive decision for the material selection. Implementing a physics-informed machine learning algorithm for this process can be a promising topic for future study.

4.2.1. Summary

This integrated experimental and computational study offers a comprehensive approach to optimising flexible membrane design for OWC wave energy converters. A critical characterisation technique combined the experimental results, mathematical models and computational simulation to identify the mechanical response of inflatable elastomers in complex deformation mode. Four different flexible membranes were characterised using this methodology. SOMR and Yeoh's models performed best for 0.2–1 mm latex and nitrile rubber, respectively, though stability limits nominal strains <1.12. Water tank testing of a 1:20 scale OWC quantified smoother frequency responses using a latex membrane. The dry test rig replicated inflation cycles up to 1.5 Hz, verifying FEA results with an excellent agreement. Simulations quantified 324% higher radial stress concentrations for silicone versus nitrile rubber at equal displacements. This indicates potential fatigue risks under cyclic loading, warranting future investigations. The integrated approach and quantitative findings significantly advance OWC membrane characterisation, enabling optimal selection. This promises major efficiency, reliability and performance improvements for next-generation OWC wave energy systems with customised soft components.

CRediT authorship contribution statement

Farhad Abad: Conceptualization, Data curation, Formal analysis, Investigation, Methodology, Software, Validation, Visualization, Writing – original draft, Writing – review & editing. **Saeid Lotfian:** Conceptualization, Data curation, Funding acquisition, Investigation, Methodology, Supervision, Writing – original draft, Writing – review & editing. **Saishuai Dai:** Data curation, Investigation, Methodology, Validation, Visualization, Writing – review & editing. **Guangwei Zhao:** Data curation, Investigation, Visualization. **Guillermo Idarraga Alarcon:** Investigation, Validation, Visualization. **Liu Yang:** Funding acquisition, Investigation, Supervision. **Yang Huang:** Investigation, Validation, Visualization, Writing – review & editing. **Qing Xiao:** Conceptualization, Funding acquisition, Investigation, Methodology, Project administration, Resources, Supervision, Validation. **Feargal Brennan:** Conceptualization, Funding acquisition, Investigation, Methodology, Project administration, Resources, Supervision, Validation, Writing – review & editing.

Declaration of competing interest

The authors declare that they have no known competing financial interests or personal relationships that could have appeared to influence the work reported in this paper.

Acknowledgment

References

[1] S. Foteinis, Wave energy converters in low energy seas: current state and opportunities, Renewable Sustainable Energy Rev. 162 (2022) 112448.

[2] A. Altunkaynak, A. Çelik, A novel Geno-fuzzy based model for hydrodynamic efficiency prediction of a land-fixed oscillating water column for various front wall openings, power take-off dampings and incident wave steepnesses, Renew. Energy 196 (2022) 99–110.

[3] M. Rosati, J. Henriques, J. Ringwood, Oscillating-water-column wave energy converters: a critical review of numerical modelling and control, Energy Convers. Manag. X (2022) 100322.

[4] L. Carlo, C. Iuppa, C. Faraci, A numerical-experimental study on the hydrodynamic performance of a U-OWC wave energy converter, Renew. Energy 203 (2023) 89–101.

[5] C. Xu, Y. He, Y. Yao, J. Zuo, Experimental and numerical study of a circular OWC with a U-shaped duct for wave energy conversion in long waves: hydrodynamic characteristics and viscous energy loss, Renew. Energy 215 (2023) 118901.

[6] A.F.O. Falcão, J.C.C. Henriques, Oscillating-water-column wave energy converters and air turbines: a review, Renew. Energy 85 (2016) 1391–1424.

[7] A.A.D. Carrelhas, L.M.C. Gato, J.C.C. Henriques, A.F.O. Falcão, J. Varandas, Test results of a 30 kW self-rectifying biradial air turbine-generator prototype, Renewable Sustainable Energy Rev. 109 (2019) 187–198.

[8] G. Moretti, G.P.R. Papini, M. Righi, D. Forehand, D. Ingram, R. Vertechy, M. Fontana, Resonant wave energy harvester based on dielectric elastomer generator, Smart Mater. Struct. 27 (3) (2018) 035015.

[9] J. Zhang, S. Ding, H. Wu, Dynamics and energy harvesting performance of a nonlinear arc-cylinder type dielectric elastomer oscillator under unidirectional harmonic excitations, Int. J. Mech. Sci. 244 (2023) 108090.

[10] S.A. Chiba, M. Waki, M. Takeshita, K. Ohyama, Possibilities of artificial muscles using dielectric elastomers and their applications, Adv. Mater. Res. 1176 (2023) 99–117.

[11] W. Sun, H. Liang, F. Zhang, H. Wang, Y. Lu, B. Li, G. Chen, Dielectric elastomer minimum energy structure with a unidirectional actuation for a soft crawling robot: design, modeling, and kinematic study, Int. J. Mech. Sci. 238 (2023) 107837.

[12] X. Li, Q. Xiao, A numerical study on an oscillating water column wave energy converter with hyper-elastic material, Energies 15 (22) (2022) 8345.

[13] I. Valizadeh, O. Weeger, Parametric visco-hyperelastic constitutive modeling of functionally graded 3D printed polymers, Int. J. Mech. Sci. 226 (2022) 107335.

[14] R.S. Rivlin, D. Saunders, Large elastic deformations of isotropic materials VII. Experiments on the deformation of rubber, Phil. Trans. Roy. Soc. Lond. Math. Phys. Sci. 243 (865) (1951) 251–288.

[15] R.W. Ogden, Large deformation isotropic elasticity–on the correlation of theory and experiment for incompressible rubberlike solids, Proceedings of the Royal Society of London. A. Mathematical and Physical Sciences 326 (1567) (1972) 565–584.

[16] C. Briody, B. Duignan, S. Jerrams, J. Tiernan, The implementation of a visco-hyperelastic numerical material model for simulating the behaviour of polymer foam materials, Comput. Mater. Sci. 64 (2012) 47–51.

[17] R. Mahnken, E. Stein, The identification of parameters for visco-plastic models via finite-element methods and gradient methods, Model. Simulat. Mater. Sci. Eng. 2 (3A) (1994) 597.

[18] S. Avril, L. Bouten, L. Dubuis, S. Drapier, J.-F. Pouget, Mixed Experimental and Numerical Approach for Characterizing the Biomechanical Response of the Human Leg under Elastic Compression, 2010.

[19] T. Xu, M. Li, Z. Wang, Y. Hu, S. Du, Y. Lei, A method for determining elastic constants and boundary conditions of three-dimensional hyperelastic materials, Int. J. Mech. Sci. 225 (2022) 107329.

[20] I. Collins, M. Contino, C. Marano, I. Masters, M. Hossain, On the influence of time-dependent behaviour of elastomeric wave energy harvesting membranes using experimental and numerical modelling techniques, Eur. J. Mech. Solid. 98 (2023) 104895.

[21] J. Yang, Z. Liao, M. Hossain, G. Huang, X. Zhou, F. Liu, A.S. Alzaidi, X. Yao, Thermo-mechanical properties of digitally-printed elastomeric polyurethane: experimental characterisation and constitutive modelling using a nonlinear temperature-strain coupled scaling strategy, Int. J. Solid Struct. 267 (2023) 112163.

[22] J.-J. Zhang, Y.-y. Sun, D.-s. Li, Y. Cao, Z. Wang, J. Ma, G.-Z. Zhao, Modeling the mechanics of graphene-based polymer composite film measured by the bulge test, J. Phys. Appl. Phys. 48 (42) (2015) 425302.

[23] R. Fu, Y. Lu, W. Cheng, Soft plasmonics: design, fabrication, characterization, and applications, Adv. Opt. Mater. 10 (1) (2022) 2101436.

[24] R. Satošek, T. Pepelnjak, B. Starman, Characterisation of out-of-plane shear behaviour of anisotropic sheet materials based on indentation plastometry, Int. J. Mech. Sci. 253 (2023) 108403.

[25] M.J. Mirnia, M. Vahdani, Calibration of ductile fracture criterion from shear to equibiaxial tension using hydraulic bulge test, J. Mater. Process. Technol. 280 (2020) 116589.

[26] F. Lo Savio, G. La Rosa, M. Bonfanti, A new theoretical-experimental model deriving from the contactless measurement of the thickness of bulge-tested elastomeric samples, Polym. Test. 87 (2020) 106548.

[27] G. Moretti, G. Malara, A. Scialò, L. Daniele, A. Romolo, R. Vertechy, M. Fontana, F. Arena, Modelling and field testing of a breakwater-integrated U-OWC wave energy converter with dielectric elastomer generator, Renew. Energy 146 (2020) 628–642.

[28] J. Portillo, K. Collins, R. Gomes, J. Henriques, L. Gato, B. Howey, M. Hann, D. Greaves, A. Falcão, Wave energy converter physical model design and testing: the case of floating oscillating-water-columns, Appl. Energy 278 (2020) 115638.

[29] G. Moretti, G.P. Rosati Papini, L. Daniele, D. Forehand, D. Ingram, R. Vertechy, M. Fontana, Modelling and testing of a wave energy converter based on dielectric elastomer generators, Proceedings of the Royal Society A 475 (2222) (2019) 20180566.

[30] M. Righi, R. Vertechy, M. Fontana, Experimental Characterization of a Circular Diaphragm Dielectric Elastomer Generator, 2014.

[31] G. Moretti, M. Righi, R. Vertechy, M. Fontana, Fabrication and test of an inflated circular diaphragm dielectric elastomer generator based on PDMS rubber composite, Polymers 9 (7) (2017).

[32] G. Moretti, G.P.P. Rosati, M. Fontana, R. Vertechy, Hardware in the loop simulation of a dielectric elastomer generator for oscillating water column wave energy converters. OCEANS 2015 - Genova, 2015, pp. 1–7.

[33] M.K. Small, W. Nix, Analysis of the accuracy of the bulge test in determining the mechanical properties of thin films, J. Mater. Res. 7 (6) (1992) 1553–1563.

[34] W.P. Jackson, Characterization of Soft Polymers and Gels Using the Pressure-Bulge Technique, California Institute of Technology, 2008.

[35] H. Bechir, L. Chevalier, M. Chaouche, K. Boufala, Hyperelastic constitutive model for rubber-like materials based on the first Seth strain measures invariant, Eur. J. Mech. Solid. 25 (1) (2006) 110–124.

[36] R. Long, C.-Y. Hui, Axisymmetric membrane in adhesive contact with rigid substrates: analytical solutions under large deformation, Int. J. Solid Struct. 49 (3–4) (2012) 672–683.

[37] A. James, A. Green, G. Simpson, Strain energy functions of rubber. I. Characterization of gum vulcanizates, J. Appl. Polym. Sci. 19 (7) (1975) 2033–2058.

[38] P. Steinmann, M. Hossain, G. Possart, Hyperelastic models for rubber-like materials: consistent tangent operators and suitability for Treloar's data, Arch. Appl. Mech. 82 (9) (2012) 1183–1217.

[39] R.S. Rivlin, Large elastic deformations of isotropic materials IV. Further developments of the general theory, Phil. Trans. Roy. Soc. Lond. Math. Phys. Sci. 241 (835) (1948) 379–397.

[40] R.W. Ogden, Non-linear Elastic Deformations, Courier Corporation, 1997.

[41] O. Yeoh, On the Ogden strain-energy function, Rubber Chem. Technol. 70 (2) (1997) 175–182.

[42] D.S. Simulia, Abaqus 6.11 Theory Manual, DS SIMULIA Corp, Providence, RI, USA, 2011, p. 524.

[43] M. Sasso, G. Palmieri, G. Chiappini, D. Amodio, Characterization of hyperelastic rubber-like materials by biaxial and uniaxial stretching tests based on optical methods, Polym. Test. 27 (8) (2008) 995–1004.

[44] M. Wissler, E. Mazza, Mechanical behavior of an acrylic elastomer used in dielectric elastomer actuators, Sensor Actuator Phys. 134 (2) (2007) 494–504.

[45] H. Somarathna, S.N. Raman, D. Mohotti, A.A. Mutalib, K.H. Badri, Hyper-viscoelastic constitutive models for predicting the material behavior of polyurethane under varying strain rates and uniaxial tensile loading, Construct. Build. Mater. 236 (2020) 117417.

[46] O.H. Yeoh, Characterization of elastic properties of carbon-black-filled rubber vulcanizates, Rubber Chem. Technol. 63 (5) (1990) 792–805.

[47] S. Chayoukhi, B. Gassoumi, H. Dhifelaoui, N. Boucherou, A. Boukhachem, M. Amlouk, A. Zghal, Structural, optical and mechanical investigations on pure and Co-doped SnO2 thin films samples, Inorg. Chem. Commun. (2023) 110391.

[48] Q. Jebur, M. Jweeg, M. Al-Waily, H. Ahmad, K. Resan, Hyperelastic models for the description and simulation of rubber subjected to large tensile loading, Arch Mater Sci Eng 108 (2) (2021) 75–85.

[49] M. Hossain, P. Steinmann, Modelling and simulation of the curing process of polymers by a modified formulation of the Arruda–Boyce model, Arch. Mech. 63 (5–6) (2011) 621–633.

[50] E.M. Arruda, M.C. Boyce, A three-dimensional constitutive model for the large stretch behavior of rubber elastic materials, J. Mech. Phys. Solid. 41 (2) (1993) 389–412.

[51] M. Drass, P. Rosendahl, M. Kraus, Coupled distortional-dilatational failure mode concept for silicone adhesives, Mech. Mater. 148 (2020) 103511.